UC Berkeley
UC Berkeley Electronic Theses and Dissertations

Title
Photon Echo Studies on Coherence Dynamics in the Photosynthetic Bacterial Reaction Center

Permalink
https://escholarship.org/uc/item/27w6006r

Author
Ryu, Seungwan

Publication Date
2013

Peer reviewed|Thesis/dissertation

Photon Echo Studies on Coherence Dynamics in the Photosynthetic Bacterial Reaction Center

by

Seungwan Ryu

A dissertation submitted in partial satisfaction of the

requirements for the degree of

Doctor of Philosophy

in

Chemistry

in the

Graduate Division

of the

University of California, Berkeley

Committee in charge:

Professor Graham R. Fleming, Chair
Professor Charles B. Harris
Professor Krishna K. Niyogi

Spring 2013

Photon Echo Studies on Coherence Dynamics in the Photosynthetic Bacterial Reaction Center

Abstract

Photon Echo Studies on Coherence Dynamics in the Photosynthetic Bacterial
Reaction Center

by

Seungwan Ryu
Doctor of Philosophy in Chemistry

University of California, Berkeley

Professor Graham R. Fleming, Chair

Photosynthetic light harvesting begins with collecting ambient photons via excitation of pigment molecules. The sophisticated design of the pigment-protein complexes is based on the cooperative network among structural motifs of pigment molecules and amino acid residues in proteins to achieve the remarkable efficiency and speed in light harvesting.

The insight from nature's photosynthetic nano-machinery can be translated to an optimal material design. The principle behind such inherent excitation energy transfer dynamics were revealed with the advance of the femtosecond laser technique. One of the examples is the quantum mechanical coherence excitation energy transfer observed by nonlinear photon echo technique.

This dissertation presents the investigation of the bacterial reaction center complexes using electronic coherence photon echo spectroscopy. The study focused on elucidating the origin of the coherence signals and identifying quantum mechanical components relevant to the excitation energy transfer. Experimental variables affecting the coherence signals were explored for the excitation energy transfer of photosynthetic bacterial reaction center. The result showed that the vibrational coherence mimics the behavior of the electronic coherence, and the lifetime is near 2 ps. A mutant bacterial reaction center was also examined to confirm the vibrational contribution. A new polarization control experiment indicates that majority of the observed vibrational coherence is from the electronic ground state.

i

Contents

List of Figures

List of Tables

Acknowledgments

It would have not been possible for me to be here without the help from all the people involved in my graduate studies. I first would like to thank my advisor, Graham R. Fleming, for all his support and introducing me the fascinating field of ultrafast spectroscopy and photosynthesis. Graham provided me perfect environment for both experimental and theoretical studies, and patiently allowed me to explore various paths.

The former and current members in the Fleming group, I have been delighted to experience and learn the diverse time and spatial scales in their research interests. I would especially thank group members who worked in the "room 3" together. We shared all the troubles and their scientific thoughts: Matthew Prantil, Yoonsoo Pang, Hohjai Lee, Jacquelyn Burchfield, Thomas Oliver, Nicholas Lewis and Julia Herz. Yuan-Chung Cheng and Akihito Ishizaki always had enlightened me with their theoretical expertise. I am deeply grateful to Hui Dong for his consistent clarity and brilliance for all the theoretical aspects. I could concentrate on my graduate studies because of the excellent admistrative support from Nancy Turley, Tiffaney Dressen and Jonathan Weld, and I truly thank them.

I also owe thanks to members of Berkeley campus outside the lab. Prof. Susan Marqusee, generously allowed her lab space for the sample preparation. Katie Hart has always been extremely helpful and kindly guided me with all the biochemical equipment. Outside of Berkeley, Prof. Steven Boxer at Stanford kindly provided bacterial reaction center strains. I was lucky to learn the excellence in protein purifications from Brett Carter in the Boxer group.

I would like especially thank Erik Hosler for his great personality, friendship, and many hours of driving for excursion.

Finally, my family and family-in-law's supports have always been an encouragement. I have been blessed with love and support from my wife, love of life, Jane. She always has been inspiring and showed great patience throughout my studies.

Chapter 1

Introduction

Understanding the precise molecular mechanisms for excitation energy transfer (EET) in photosynthetic membrane protein architecture is particularly crucial for identifying key principles necessary to the design and control materials at the quantum level for efficient solar energy utilization. In the past several years, the quantum mechanical nature of photosynthetic EET was observed [1, 2, 3, 4] by ultrafast photon echo spectroscopy, and suggested as a potential key mechanism for the efficient light harvesting processes. In this dissertation, the origin of the coherence dynamics in EET is investigated by conducting ultrafast photon echo experiments on bacterial reaction centers. Ultrafast photon echo spectroscopy was designed to be particularly sensitive to the electronic coherence, was used therefore for the studies.

1.1   Photosynthesis

Photosynthesis is one of the most fundamental metabolic processes, in which sunlight is transformed into chemical energy. Photosynthetic processes can be divided into two stages - light reactions and dark reactions. In the light reactions, photons are harvested by pigment molecules to trigger a charge separation that creates a proton gradient across the membrane in photosynthetic organisms. The proton gradient drives synthesis of ATP (adenosine triphosphate), which is used in the dark reactions for biochemical synthesis.

Details of whole photosynthetic process may differ from species to species, but the light reactions always start with absorption of incident sunlight by pigment molecules in photosynthetic protein complexes. Two classes of proteins are involved in light reactions - light harvesting antennas and reaction centers. Light harvesting antenna proteins absorb light energy and transfer excitation energy to reaction centers, where charge separation transforms light energy into chemical energy. Photosynthetic organisms have perfected their protein network machinery to achieve great speed (hundreds picoseconds) and high quantum efficiency in energy transfer and charge separation[5].

1.1.1   Photosynthetic Pigments

The majority of photosynthetic pigments are chlorophylls (Chls), cyclic tetrapyrroles carrying a isocyclic five-membered ring. Figure 1.1 shows the chemical structure of chlorophyll a (Chl$a$) and bacteriochlorophyll a (BChl$a$) molecules. Nearly 100 different Chls are known today, but the structure of aromatic chlorin macrocycle is the basis for the electronic properties of Chls. The optical properties of Chls can be described by the four-orbital model proposed by Gouterman[6]. In this model,
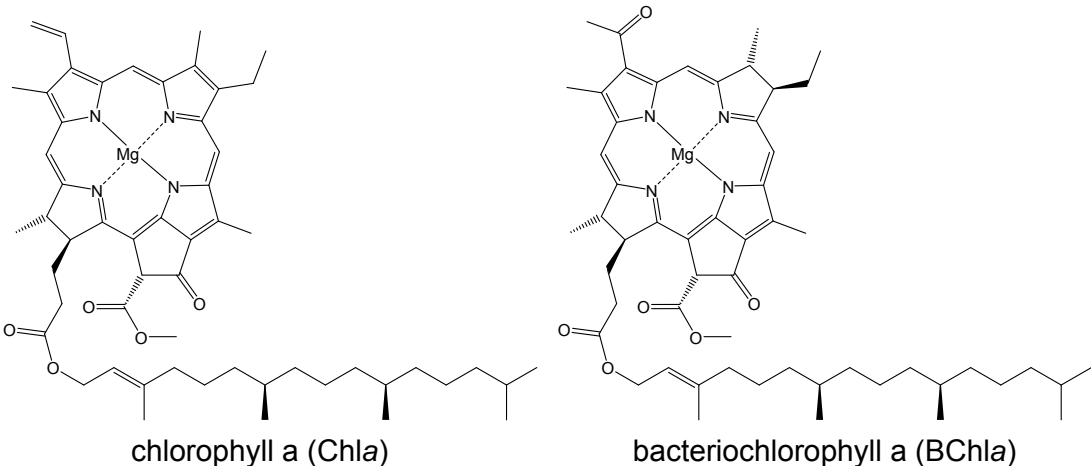
Figure 1.1: Chemical structures of chlorophyll a and bacteriochlrophyll a

electronic transitions arise from the linear combination of one-electron promotions between the two highest occupied (HOMO and HOMO-1) and two lowest unoccupied molecular orbitals (LUMO and LUMO+1). The two lowest singlet excited states are denoted as Q_x and Q_y. The first excited state (Q_y) and the ground state are often further simplified to a two-level system to describe multichromophoric systems. Different side chains attached to the chlorin ring alter the transition energies for different chlorophylls leading to various action spectra. For example, Chl*a* has a Q_y absorption maximum around 660 nm while BChl*a* has a Q_y transition centered around 750 nm due to the reduced conjugation length.

Another class of photosynthetic pigment is pheophytins (Phes). Pheophytins are structurally identical to chlorophylls except they are missing the central Mg^{2+} metal ions. Also pheophytins have higher reduction potentials than chlorophylls (by about 300 mV) due to the decreased electron density from lacking Mg^{2+} ion [7]. Thus pheophytins play an essential role as electron acceptors in the charge separation process occurring in reaction center proteins.

1.1.2 Photosynthetic Pigment-Protein Complexes

The photosynthetic apparatus consists of several pigment-protein complexes (PPCs) located in the membrane. One common feature of all photosynthetic membrane is the ratio of reaction center proteins to light harvesting antenna complexes. The light harvesting structure of photosynthetic membranes consists of a series of reaction centers which are each supported by many light harvesting antenna. The light

Electronic Coupling   Electron-Phonon Coupling

Molecular sites   Excitonic states

Energy

$d_{n\xi}$ Q_ξ
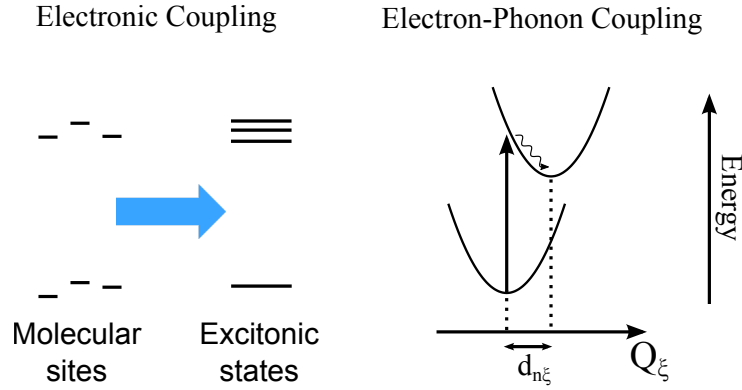
Figure 1.2: (Left) Electronic couplings lead to delocalized excitonic states. (Right) Electron-photon coupling lead to broadening of the absorption lineshape

harvesting antenna relay the excitation energy toward their respective reaction centers for photochemistry. On the molecular level, energy transfer is mediated by the excited states of pigment molecules, mostly (bacterio) chlorophylls, in photosynthetic PPCs.

Photosynthetic pigment molecules are non-covalently bound to proteins, forming functional photosynthetic PPCs. The protein matrix holds light-absorbing pigment molecules in the proper positions, where interchromophoric spacings are optimized for the efficient energy transfer and charge separation.[4]. The excited state transition energy of each pigment is uniquely configured to achieve its functionality via interactions with surrounding chromophores and amino acids from the protein. The chromophore's noncovalent interactions such as hydrogen bonding with nearby amino acids shift the electronic transition energies via the electrochromic effect[8].

1.1.3 Excitons

(Bacterio) Chlorophylls in PPCs are arranged in close proximity (less than 10Å)[9], resulting in strong intermolecular electrostatic interactions referred to as electronic couplings. Electronic coupling between chromophores lead to the formation of collective excitations delocalized over several molecules in the complex. Such excitation are named Frenkel excitons, where excitations are constrained to a few molecules. Frenkel excitons have been widely used to describe optical properties of molecular aggregates and photosynthetic PPCs including excitation energy transfer. Another type of excitons are found primarily in inorganic semiconductor materials, where the excitons have large radius due to high dielectric constants and is referred to as

Wannier-Mott excitons, which is not relevant to the current discussion.

Excited state transition energies are also affected by environmental interactions, and is known as system-bath or electron-phonon coupling. The physical origin of system-bath coupling is the vibrational degrees of freedom of diverse nuclear motions such as intramolecular vibrations, hydrogen bonding networks and coordination of amino acid residues. Despite the diverse physical mechanisms, system-bath couplings are not explicitly accounted for, but are rather averaged over in the theoretical description of Frenkel excitons. This is justified by virtue of the nuclear dynamics being slower than the electronic dynamics (Born-Oppenheimer approximation). Therefore, system-bath couplings can be considered as static disorders which stochastically modulate electronic transition energies. This results in a broadening of the absorption lineshapes.

The excitonic Hamiltonian for a photosynthetic PPC with N pigment molecules can be generally expressed as follows [10, 11, 8]: where H_{system} describes the electronic excitation of molecule n with site energy ε_n and intermolecular electronic couplings are determined by J_{nm}. The form of $H_{\text{system-bath}}$ represents linear system-bath coupling with a collective bath coordinate $\mathbf{Q}_\xi$ and dimensionless electron-phonon coupling constants $d_{n\xi}$ for the nth molecule. The vibrations in the bath (H_{bath}) are described by harmonic oscillators where T_{nuc} is the kinetic energy of nuclei.

$$H_{\text{PPC}} = H_{\text{system}} + H_{\text{system-bath}} + H_{\text{bath}} \tag{1.1}$$

$$H_{\text{system}} = \sum_{n=1}^{N} \varepsilon_n |n\rangle \langle n| + \sum_{n \neq m} J_{nm} |n\rangle \langle m| \tag{1.2}$$

$$H_{\text{system-bath}} = \sum_{n=1}^{N} \sum_{\xi} \hbar\omega_\xi d_{n\xi} \mathbf{Q}_\xi |n\rangle \langle n| \tag{1.3}$$

$$H_{\text{bath}} = \sum_{\xi} \hbar\omega_\xi \mathbf{Q}_\xi^2 |n\rangle \langle n| + T_{nuc} \tag{1.4}$$

1.2 Bacterial Reaction Center

Reaction center complexes are where solar-to-chemical photochemistry occurs. All reaction centers carry out electron transfer reactions, leading toa trans-membrane electrochemical gradient which drives subsequent biochemical processes. Unlike light harvesting complexes, which show great diversity in structural architecture, the arrangement of core pigments in reaction centers is conserved for all photosynthetic organisms.[12] (See Figure 1.3) Reaction center complexes are divided into two classes
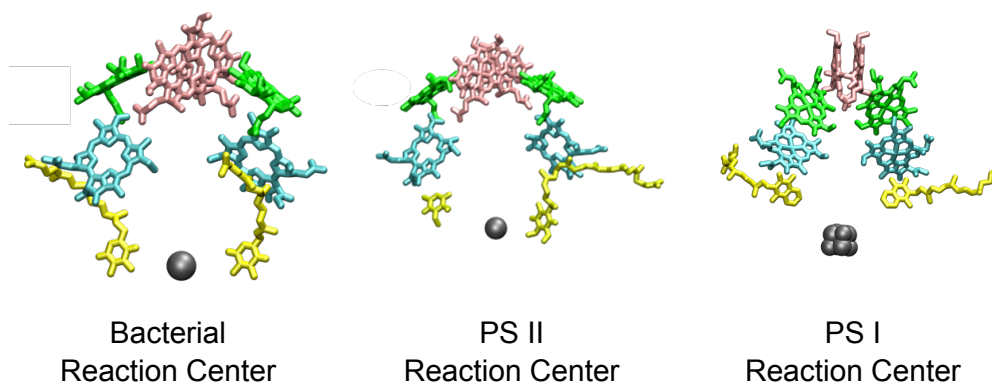
Figure 1.3: The core molecular arrangements of chromophores connected with primary charge separations of bacterial, PS II and PS I reaction centers.

based on their terminal electron acceptor. Reaction centers containing Fe_4S_4 clusters are classified as type-I reaction centers, while type-II reaction centers utilize quinones as an electron acceptor.[13]

Bacterial reaction centers (bRC), especially the one from purple bacteria *Rhodobacter sphaeroides*, can be separated from antenna complexes by biochemical techniques and isolated without losing its photochemical functions. In combination with its available crystal structure information, the purple bacterial reaction center has been a superb model system for studying biological energy and electron transfer in photosynthesis. Another advantage is the distinctive absorption lineshapes, facilitating spectroscopic interpretation of reaction dynamics.

The pigment molecules in bRC from *Rhodobacter sphaeroides* are arranged with pseudo-C2 symmetry consisting of two branches called L and M that represent the protein subunit around six pigment molecules. These pigments are: a pair of BChls forming a dimer referred to as the special pair (P), with two symmetrically neighboring accessory BChls (B_L and B_M) and two bacteriopheophytins (BPhys; H_L and H_M) next to the accessory BChls. These six chromophores exhibit three well-separated Q_y absorption bands in the near-infrared region.
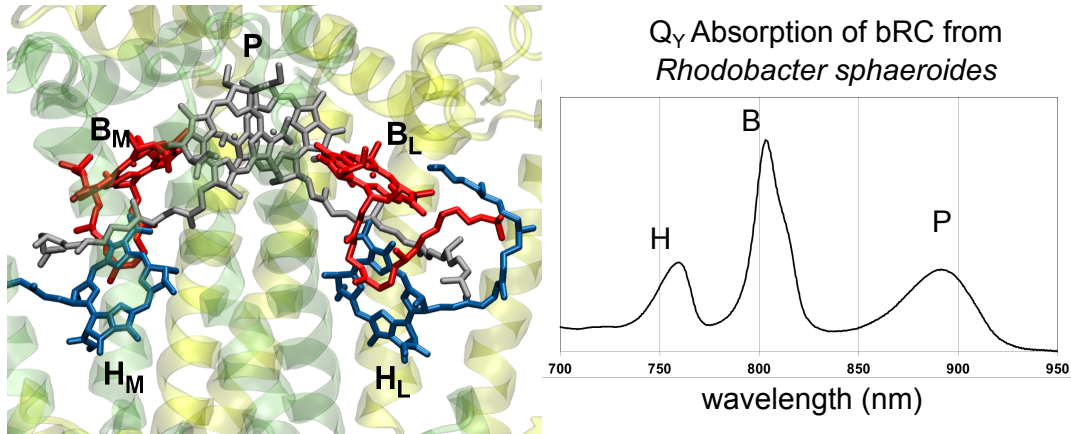
Figure 1.4: The crystal structure of bacterial reaction center from *Rhodobacter sphaeroides* and its Q_Y absorption spectrum. The three separated absorption bands are ideal for spectroscopic studies. The crystal structure is from (PDB ID: 1PCR).

1.3 Photon Echo Spectroscopy

1.3.1 Femtosecond Nonlinear Optical Spectroscopy

The timescale for fundamental chemical processes such as molecular vibrations, solvation, energy / electron transfer spans from tens of femtoseconds to hundreds of picoseconds. Experimental observations of such ultrafast molecular processes have been developed alongside the advent of pulsed laser techniques. Much progress has been achieved in the generation and characterization of stable and tunable femtosecond laser sources based on the modelocked Ti:Sapphire solid state laser system.

The technique discussed in this work is in the field of nonlinear spectroscopy, more specifically on third order nonlinear processes. Upon irradiation by light, electron distributions in a material changes according to the electronic structure, resulting changes in macroscopic polarizations (P). The polarization response of a material can be expanded in powers of the electric field strength, giving

$$P = P^{(1)} + P^{(2)} + P^{(3)} + \cdots \tag{1.5}$$

where $P^{(1)}$ represents linear response of system, such as light absorption. The second order polarization terms ($P^{(2)}$) disappear when the material contains inversion symmetry. Thus a second order response is important for investigations of surface properties or nonlinear optical properties of crystals with a certain structure. Due to the inversion symmetry in isotropic solutions, where molecules of interest are

randomly oriented, third order polarizations $(P^{(3)})$ are often the lowest nonlinear processes accessible for chemical processes occuring in condensed phase.

In general, $P^{(3)}$ can be calculated by using the nonlinear response functions, $R(t_3, t_2, t_1)$, as following.

$$
\begin{aligned}
P^{(3)}(t) &= \int_0^\infty dt_3 \int_0^\infty dt_2 \int_0^\infty dt_1 R(t_3, t_2, t_1) \\
&\quad E(t - t_3) E(t - t_3 - t_2) E(t - t_3 - t_2 - t_1)
\end{aligned}
\tag{1.6}
$$

Here $E(t)$ represents an electric field that interacts with a material at given time t, thus all the microscopic information of the investigated system are embedded in the response functions. Multiple interactions with electric fields (i.e. laser fields) and corresponding material responses are conveniently described by the double-sided Feynman diagram. One double-sided Feynman diagrams represent one microscopic pathway that the system evolves through according to the density matrix elements as a result of interaction with external electric fields.

Experimental investigations of the third order polarization $(P^{(3)})$ is more generally referred to as *four wave mixing* experiments. Here "wave" is related to an electric field, implying four electric fields are involved. Three of these four electric fields (i.e. waves) refer to the three applied external fields, (e.g. applied three separate femtosecond laser pulses) and are generally labeled as $\mathbf{k_1}$, $\mathbf{k_2}$ and $\mathbf{k_3}$. The fourth wave is the stimulated signal electric field generated by the material's third order polarization response and labeled $\mathbf{k}_s$, whose direction of emission is determined by the condition of the conservation of of momentum called the phase matching directions (Equation 1.7).

$$
\mathbf{k}_s = \pm \mathbf{k_1} \pm \mathbf{k_2} \pm \mathbf{k_3}
\tag{1.7}
$$

As indicated in Equation 1.7, eight total phase matching directions are possible. Also, in time domain experiments, the order of three external fields can be permutated. In theory, the combination of pulse ordering and phase matching directions result in at least 48 different Feynman diagrams. However in the practical employment of four wave mixing experiments, researchers control the beam geometry, pulse orderings, and resonance conditions to restrict the number of Feynman diagrams contributing to the signal[14].

1.3.2   Photon Echo

Photon echo stimulated emission arises from reversing the dephasing of the initial coherent excitations. In a molecular system approximated to two-levels composed
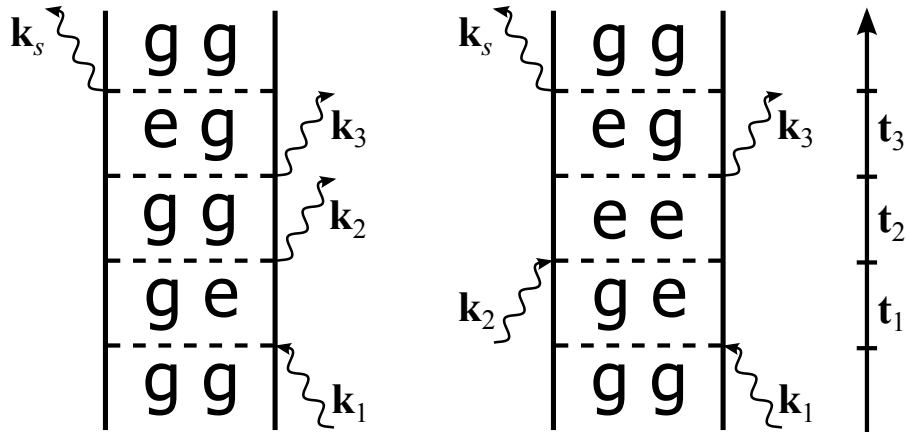
Figure 1.5: Double-sided Feynman diagrams for a three-pulse photon echo. The arrow on the far right indicates time evolution and delays between pulses. During t_1 the system is in $|g\rangle \langle e|$ coherence and dephasing occurs. t_2 represents the population time, and rephasing occurs in t_3.

of electronically ground ($|g\rangle$) and excited states ($|e\rangle$), the initial equilibrium state can be described by a density matrix element of ground population state ($|g\rangle \langle g|$). An interaction with external electric field prepares the system in a coherent super-position state, coherence ($|g\rangle \langle e|$). The coherently excited group of transition dipole moments experiences dephasing due to various fluctuations caused by the environment until the second external electric field interacts with system. After the second field, the system population is either in ground or excited states ($|g\rangle \langle g|$ or $|e\rangle \langle e|$). Since both Bra and Ket states are in the same state, the phase factors leading to dephasing vanishes during the time evolution in a population state. The third external field returns the system to a coherent state. If there is an ensemble of coherently excited molecules which retained the initial phase relationship, the collective rephasing process produces a macroscopic photon echo signal in the phase matched direction ($\mathbf{k}_s$).

The above described process can be summarized by double-sided Feynman diagrams in Figure 1.5. The ability of the system to rephase during the second coherence time (t_3) depends on the changes in chromophores' transition energies during the population time t_2. Thus photon echo is sensitive to the transition frequency fluctuations caused by electron-phonon coupling to the environment (e.g. protein or solvating molecules), making the photon echo a valuable observable for investigating disordered systems.
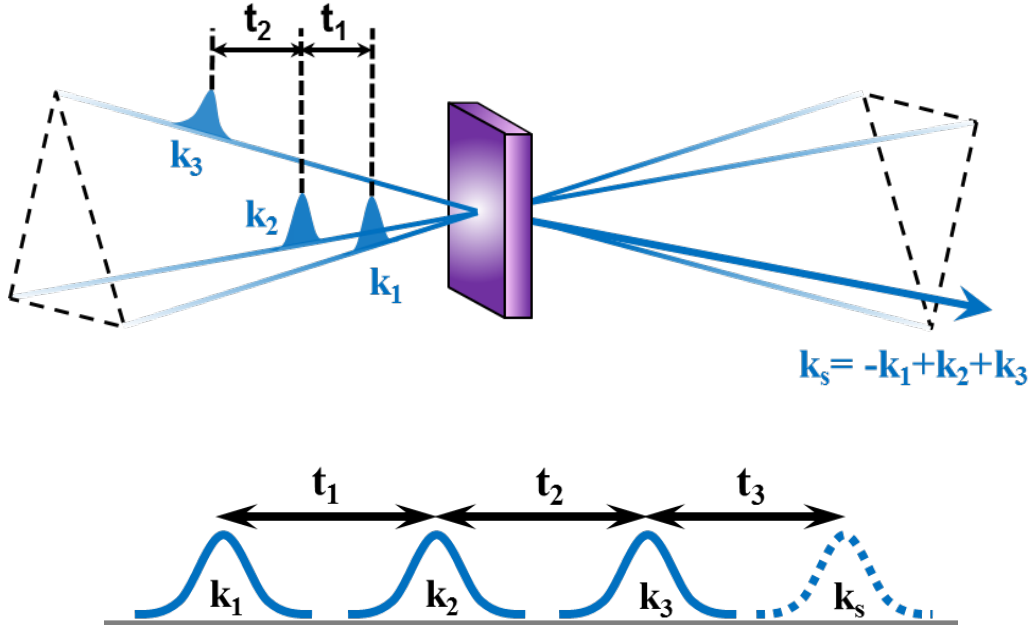
Figure 1.6: Experimental scheme for a one-color three pulse photon echo peak shift (1C3PEPS) measurement.

1.3.3 One-Color Three Pulse Photon Echo Peak Shift (1C3PEPS)

Excited state transition frequencies are influenced by the many nuclear coordinates of a molecule by electron-phonon coupling. Although the overall magnitude of such a coupling strength can be estimated by either the Stokes shift or the width of absorption lineshape, insight into the ultrafast dynamic responses of nuclear motions induced by electronic excitation cannot be obtained by steady state information. One-color three pulse photon echo peak shift (1C3PEPS), where the generated photon echo field intensity is detected with time integration, provides useful information about rearrangement dynamics of the surrounding environment (e.g. solvation)[15, 16].

As the time delay between the three pulses are varied, the intensity of the generated photon echo signal field will change as a function of two time delays (t_1 and t_2). The echo signal field itself also has time dependence (t_3), but this time is integrated with homodyne intensity detection. Thus the observed signal intensity is recorded as a function of coherence time (t_1) and population time (t_2) (Equation 1.8).
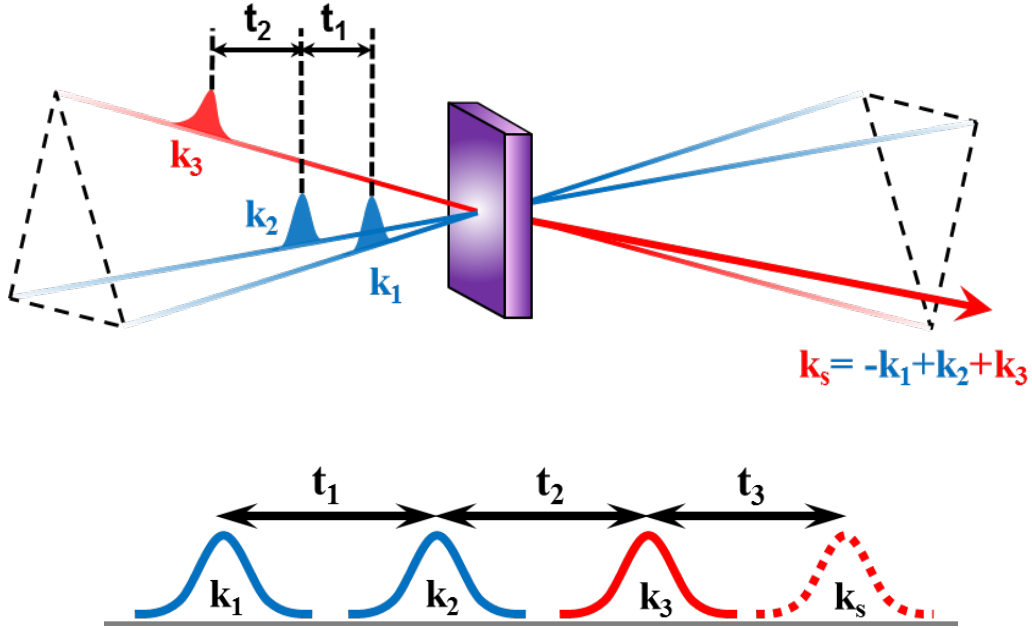
Figure 1.7: Experimental scheme for two-color three pulse photon echo peak shift (2C3PEPS) measurement.

$$I_{\text{signal}}(t_1, t_2) = \int_{-\infty}^{\infty} dt_3 \left| E_{\text{echo}}(t_1, t_2, t_3) \right|^2 \tag{1.8}$$

At a given population time t_2, the integrated echo signal profile peaks at a positive t_1 value in the presence of a rephasing capability in the system. The peak shift (τ^*) value is defined as the coherence time (t_1) at which the integrated signal is the highest. It was found that the one-color peak shift profile, $\tau^*(t_2)$, closely follows the transition frequency correlation function, which contains all the essential information on fluctuations of transition frequencies.

1.3.4 Two-Color Three Pulse Photon Echo Peak Shift (2C3PEPS)

Investigation of transition frequency correlations can be extended to the correlation between the two separate spectral regions. Instead of using the same wavelength for three laser pulses, the third pulse can be chosen differently from the first two pulses (Figure 1.7). This technique is called the two-color three pulse photon echo peak shift (2C3PEPS), and measures how a transition frequency fluctuation in
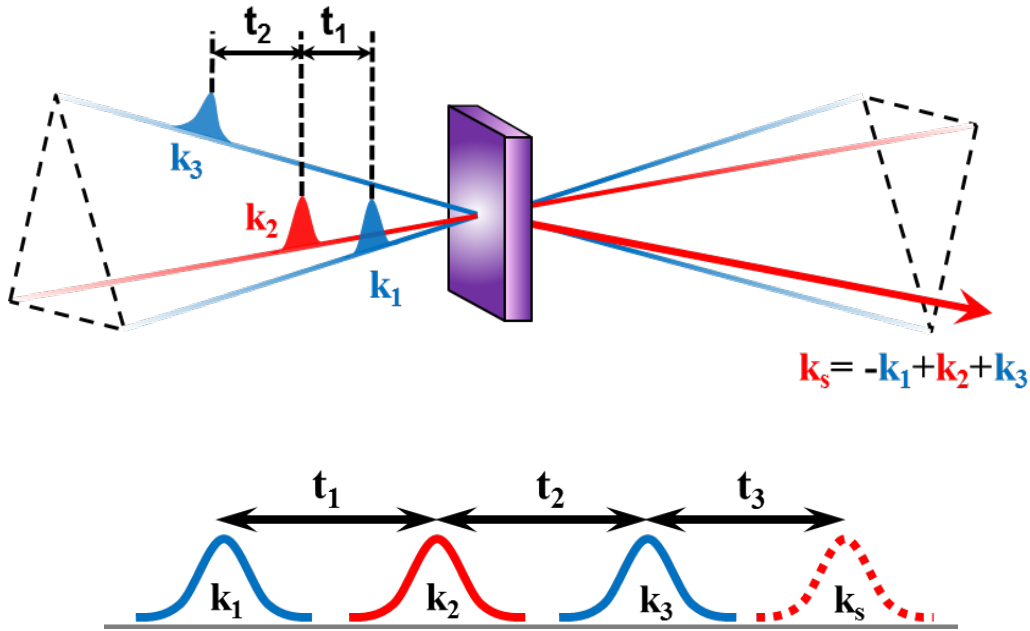
Figure 1.8: Experimental scheme for a two-color electronic coherence photon echo (2CECPE) measurement.

one spectral region (determined by the first and second pulses) is related to another spectral region (determined by the third pulse). It was shown that 2C3PEPS is able to determine the electronic coupling between two different excited states [17, 18]and detect correlated spectral shifts[19].

1.3.5 Two-Color Electronic Coherence Photon Echo (2CECPE)

Electronic coupling between two chromophores leads to coherent energy transfer between them. For the past several years, the coherent superposition between two excitonic states during energy transfer was observed in multiple photosynthetic PPCs. Most observations relied on beating features in the cross-peak of two-dimensional (2D) electronic spectroscopy[1, 2]. However, the information from the 2D electronic spectroscopy can sometimes be difficult to interpret and obtain because the signal is intrinsically the combination of many pathways related to the population dynamics.

A new technique named two-color electronic coherence photon echo (2CECPE) was developed to selectively investigate the quantum coherence phenomena [3]. As shown in Figure 1.8, the first and second pulses have different center wavelengths

to excite two separate spectral regions and prepare a coherence between them. The signal is generated only if the system contains coherent coupling between the two spectral regions. Any additional features in the coherence signal (e.g. oscillations) arise when additional vibrational modes are associated with the coherence, thus allowing a more detailed investigation of the quantum coherence properties. The signal intensity for a quantum coherence is generally weaker than population related signals. This is presumably due to the nature of electronic coherence being inherently susceptible to dephasing processes.

Information from 2CECPE technique can be further refined by the polarization control of laser pulses. The experimental implementation and optimization strategy for the 2CECPE signal is discussed in Chapter 2.

Chapter 2

Experimental Techniques

2.1 Introduction

Excitonic quantum coherences observed in photosynthetic systems have intrigued many related research fields, e.g. quantum information[20]. Two-color electronic coherence photon echo spectroscopy can isolate the coherence pathway to facilitate analysis of evolution of prepared coherence in the system. Additional polarization control of individual pulses provides a means to further narrow the contributing pathways. In this chapter, the polarization scheme for the 2CECPE will be introduced and the Feynman diagrams for a simple 4 level system are described.

Although 2CECPE can be powerful experimental technique to study coherence, it is often the case that the coherence related signal is too weak to detect with a reliable signal-to-noise ratio. The strategies implemented in the experimental setup to optimize and enhance 2CECPE signal will be discussed along with the polarization dependent 2CECPE.

2.2 Polarization Control in 2CECPE

2.2.1 Polarization Prefactor with Orientational Average

Individual control of the polarization direction of the excitation laser pulses used in 2D electronic spectroscopy provided further capability to distinguish the pathways contributing to the signal. Orientational effects in spectroscopy have been an important part of signal detection, and identifying different components of system dynamics contributing to signals. In three pulse photon echo experiments, each light-matter interaction can be considered as a dot product between the light electric field polarization vector and the sample transition dipole vector. In a multichromophoric system such as photosynthetic PPC, the transition dipole moments of composing molecules are oriented in fixed angles between each other. However, in ensemble measurement where there are many such protein molecules, the isotropic rotational average effect needs to be accounted for to properly describe the polarization dependence of the signals.

$$
\left\langle \left(\hat{\alpha} \cdot \hat{E}_a \right) \left(\hat{\beta} \cdot \hat{E}_b \right) \left(\hat{\gamma} \cdot \hat{E}_c \right) \left(\hat{\delta} \cdot \hat{E}_d \right) \right\rangle
$$

$$
= \quad \frac{1}{30} \begin{pmatrix} \cos\theta_{ab}\cos\theta_{cd} \\ \cos\theta_{ac}\cos\theta_{bd} \\ \cos\theta_{ad}\cos\theta_{bc} \end{pmatrix}^T \begin{pmatrix} 4 & -1 & -1 \\ -1 & 4 & -1 \\ -1 & -1 & 4 \end{pmatrix} \begin{pmatrix} \cos\theta_{\alpha\beta}\cos_{\gamma\delta} \\ \cos\theta_{\alpha\gamma}\cos_{\beta\delta} \\ \cos\theta_{\alpha\delta}\cos_{\beta\gamma} \end{pmatrix} \quad (2.1)
$$

$$
= \quad \frac{1}{30} \left\{ \cos\theta_{\alpha\beta}\cos_{\gamma\delta} \left(4\cos\theta_{ab}\cos\theta_{cd} - \cos\theta_{ac}\cos\theta_{bd} - \cos\theta_{ad}\cos\theta_{bc} \right) \right.
$$

$$+ \cos\theta_{\alpha\gamma} \cos_{\beta\delta} \left(- \cos\theta_{ab} \cos\theta_{cd} + 4 \cos\theta_{ac} \cos\theta_{bd} - \cos\theta_{ad} \cos\theta_{bc}\right)$$
$$+ \cos\theta_{\alpha\delta} \cos_{\beta\gamma} \left(- \cos\theta_{ab} \cos\theta_{cd} - \cos\theta_{ac} \cos\theta_{bd} + 4 \cos\theta_{ad} \cos\theta_{bc}\right)\} \qquad (2.2)$$

Equation 2.1 and 2.2 are the general algebraic expressions for the orientationally averaged prefactor for a Feynman diagram pathway[21, 22]. The indexes of a, b, c, d are the light polarizations in the lab frame and α, β, γ and δ are the excited state transition dipole moments in the molecular frame. For example, θ_{ab} represents the relative polarization angle difference between $\hat{E}_a$ and $\hat{E}_b$ and $\theta_{\alpha\beta}$ represents angle between two transition dipoles of α and β. The angle between transition dipole moments can be expressed more explicitly as in Equation 3.2.

$$\hat{\mu}_\alpha \cdot \hat{\mu}_\beta = |\mu_\alpha| \, |\mu_\beta| \cos\theta_{\alpha\beta} \qquad (2.3)$$

The calculated polarization prefactor can be used to design polarization sequences to selectively suppress or enhance certain Feynman diagram pathways.

2.2.2 Polarization Dependent 2CECPE

A coupled dimer system will be considered as an example in this section. Figure 2.1 shows the schematic diagram for a coupled dimer. In the 2CECPE experiment, two different colors of laser pulses are used to ensure that one pulse interacts only with one excitonic state. However, as seen in Figure 2.1 (b), the energy of a higher vibrational state ($|\beta_1\rangle$) of the lower excitonic state ($|\beta\rangle$) can coincide with the energy of upper excitonic state ($|\alpha_0\rangle$).

All possible double-sided Feynman diagrams based on the above excitonic model are shown in Figure 2.2. Under the frame of the exciton-vibrational model, six different Feynman diagrams are available, and the physical meaning of each are very different.

Control over the polarization of the incident laser pulses offers a possibility to further isolate the pathways. Table 2.1 shows the calculated polarization prefactors for three difference polarization configurations. Sequence <1> is the case in which all the excitation beam polarizations are set parallel to each other, and three pulse photon echo experiments are typically performed in this configuration. Sequence <2> suppresses all the pathways except the electronic coherence pathway, and often referred as the coherence-specific sequence. For example, when all interactions are associated with the same transition dipole, such as the R_6 pathway in Figure 2.2, the zero polarization prefactor effectively minimizes the contribution from this pathway. The pathways shown in Figure 2.2 indicate that polarization control is necessary
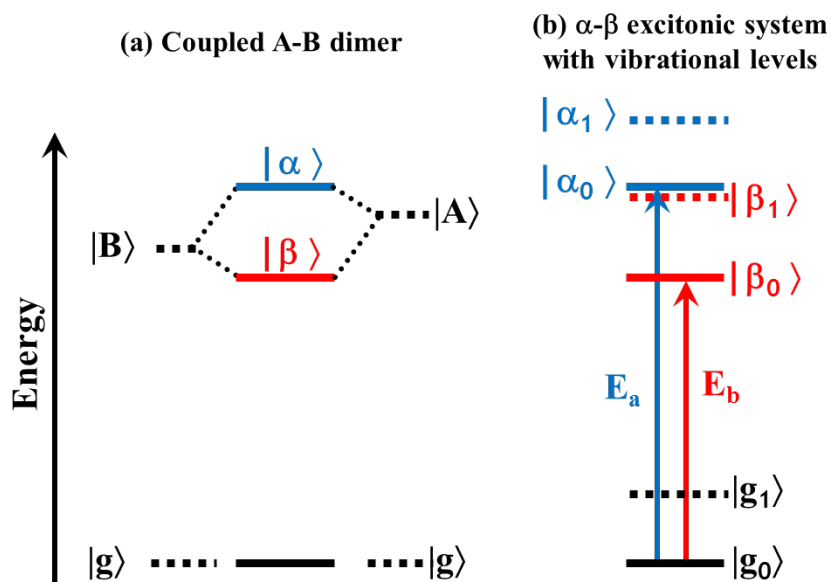
Figure 2.1: Schematic energy diagram for a dimer of molecule A and B. E_a and E_b indicate the center wavelength of the two laser pulses chosen to exclusively excite exciton α and β (a) A and B excited states form excitonic levels α and β. Double excitonic states are not shown. (b) α-β excitonic system with explicit consideration of vibrational levels. For β exciton, a vibrational mode which lies near α exciton state was chosen.
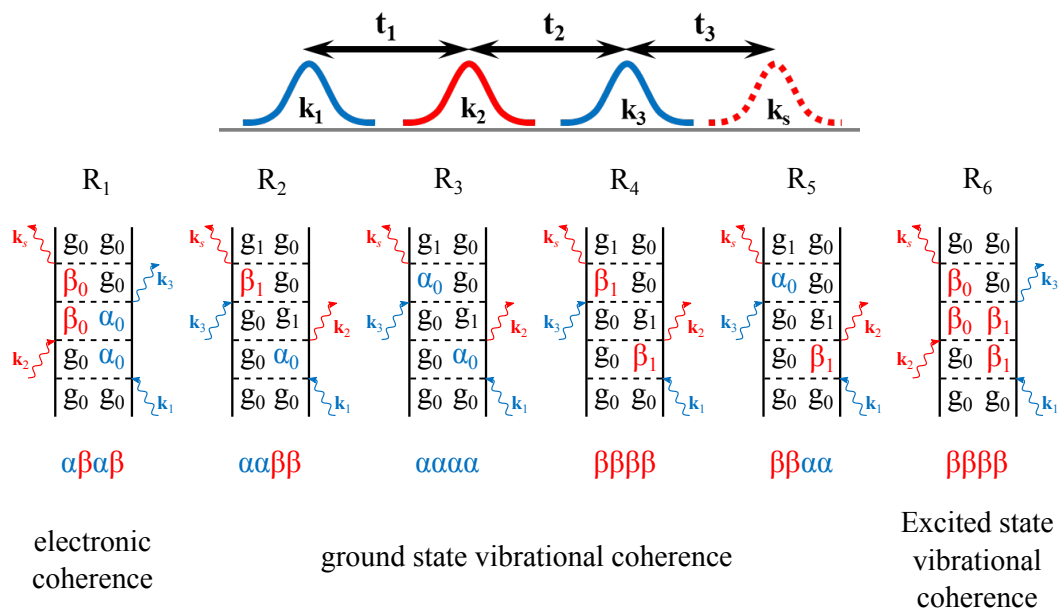
Figure 2.2: Accessible Feynman diagram pathways by the 2CECPE pulse sequence. The four Greek letters below each diagram indicate the four transition dipole moments associated to the pathway in the order of interaction. The physical processes the system experiences during t_2 time (delay between second and third pulse) are noted.

Table 2.1: Calculated polarization factors from $\left\langle \left(\hat{\alpha} \cdot \hat{E}_a \right) \left(\hat{\beta} \cdot \hat{E}_b \right) \left(\hat{\gamma} \cdot \hat{E}_c \right) \left(\hat{\delta} \cdot \hat{E}_d \right) \right\rangle$. The two transition dipole moments were assumed to be orthogonal. (i.e. $\theta_{\alpha\beta} = \pi/2$)

	Polarization Configuration				Feynman Pathways: $\alpha\beta\gamma\delta$		
	a	**b**	**c**	**d**	$\alpha\alpha\alpha\alpha/\beta\beta\beta\beta$	$\alpha\alpha\beta\beta/\beta\beta\alpha\alpha$	$\alpha\beta\alpha\beta$
<1>	0	0	0	0	1/5	1/15	1/15
<2>	$\pi/4$	$-\pi/4$	$\pi/2$	0	0	0	1/12
<3>	$\pi/4$	$\pi/2$	$-\pi/4$	0	0	1/12	0
	Relevant Feynman Diagram:				R_3, R_4, R_6	R_2, R_5	R_1

even for 2CECPE experiment to obtain a pure electronic coherence signal. Sequence <3> can extract complementary information to the coherence specific sequence.

2.3 Optimization of 2CECPE Signal

2.3.1 Scattering Removal

Nonlinear phenomena are inherently weaker than the first order processes. The fundamental part in nonlinear spectroscopy experiments is the focusing of femtosecond pulses onto a system of interest. As the system experiences ultrashort laser pulses in a very small volume, the possibility of nonlinear interaction is maximized leading to the strongest signal generation. Unfortunately, all nonlinear experiments carried by focusing laser pulses on a sample cannot avoid contamination from scattering process. Such a problem can be usually ignored when the generated signal is much stronger than the scattering, but this is not the case for the dection of a weak coherence signal.

The detection system for 2CECPE uses photomultiplier tubes (PMTs) to sensitively detect echo signal photons, but this also means it is sensitive to the photons from scattering process. Although scattered photons are randomly oriented, there is always a small portion that travels in the same direction as the phase matched photon echo signal, and those are easily detected by PMTs.

In the 2CECPE setup used in this work, scattering contamination was minimized by two filtering stages. The first filtering was achieved by simply placing an adjustable iris along the signal propagation path. The iris was mounted on two translational micrometer stages for optimal positioning. The iris opening diameter can be controlled to match the signal beam diameter as exactly as possible in combination
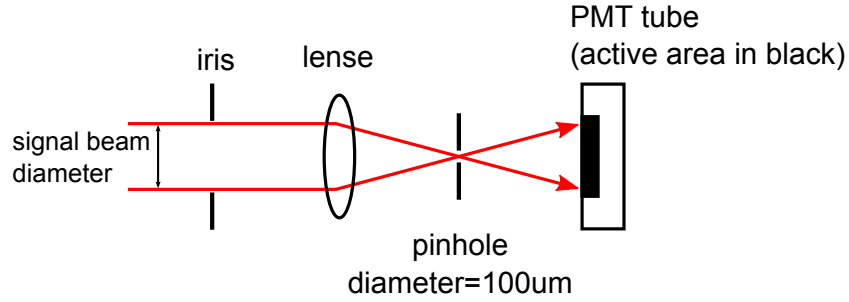
Figure 2.3: The filtering scheme for scattering removal in 2CECPE detection system

to the fine adjustment of the iris position.

The second filtering of scattering was done by the spatial filtering of signal. Figure 2.3 shows the schematic diagram for the setup. When the echo signal beam is passed through a pinhole with a diameter of 100 μm, any scattered photons travelling with slight deviation from the signal propagation direction will be blocked by the pinhole. The tolerance of scattered photons can be further lowered by using a smaller diameter pinhole, but the detected number of photons will simultaneously decrease.

2.3.2   Optimal Spatial Pulse Overlap

An additional difficulty in the two-color experiments results from the the control of laser pulses with different properties. Two laser pulses with different center wavelengths can be prepared by two independent optical parametric amplifiers (OPAs), or one OPA output can be used together with the fundamental output from the regenerative amplifier. In either cases, the stability and matching of the beam sizes between two laser pulses travelling along different optical paths are critical to obtaining a high signal-to-noise ratio.

The diameter of a laser beam is controlled by a collimation setup, composed to two lenses (or curved mirrors). However, the determination of the lens positions are usually not tightly controlled and performed by the simple visualization of beam on a beam profiling camera. However, such adjustment do not guarantee identical diameters of the focal spot sizes for two differently colored laser pulses. The focal spot diameter defines the volume of nonlinear interaction between the investigated sample and laser pulses, thus determining the amount of photon echo signal generation.

The maximum spatial overlap of all the three pulses at the sample position was achieved by placing a 50 μm pinhole on XYZ-axis stage at the focal point. The pulse power through the pinhole is maximized by adjusting the pinhole position. To

match and tightly control the focal spot diameter of two laser beams with different colors, one of the collimation lenses was mounted on a micrometer stage. Varying the micrometer change the collimation slightly and a 50 μm pinhole was enough to detect small changes in laser pulse power after the pinhole. Fine adjustment of the collimation for one laser color ensured the same focal volume for all three laser pulses with two different wavelengths.

Chapter 3

Origin of the Long-Lived Coherence Signal in Photosynthetic Bacterial Reaction Center

3.1 Introduction

Photosynthesis is a fundamental solar to chemical energy conversion process mediated by a sophisticated pigment-protein complex network. Ambient light photons excite pigment molecules creating excitons which migrate toward a reaction center complex, where light-induced charge separation transforms light energy into chemical energy with near unity quantum efficiency. X-ray crystallographic studies provid the structural foundation for properties of photosynthetic pigment-protein complexes, while the detailed molecular understanding of electronic and vibrational couplings governing the dynamics of excitation energy transfer in PPCs are still unclear.

The evidence for the coherent nature in excitation energy transfer (EET) has been observed in the past several years with the development of photon echo four-wave mixing techniques, especially two-dimensional electronic spectroscopy (2DES) and two-color electronic coherence photon echo spectroscopy. Studies on various photosynthetic EET processes have shown that oscillating features observed by two-dimensional electronic spectroscopy (2DES) can be explained as an excitonic coherence during EET process [1, 10, 2, 11]. Also, a coherence photon echo study on the bacterial reaction center suggested the electronic coherence is protected by the correlated fluctuation of chromophore's surrounding protein environment [3]. Although the existence of coherently excited components has been found universally in photosynthetic PPCs, the questions remain about the exact molecular details of them. Those observed oscillations interestingly persisted over a duration much longer (nearly 2 ps) than theoretical predictions of electronic coherences (several hundreds femtoseconds), and are always accompanied by other frequencies indicative of the associated vibrational modes. This naturally raises the question about the role of vibrational modes in electronic coherence, and to what extent the coherence signal is composed of the vibrational contributions.

Several studies focused on identifying the vibrational components in the coherence signal, but unambiguous experimental evidence has not yet been reported. Here we demonstrate that the ground state vibrational coherence, prepared via nonadiabatic vibrational-electronic mixing[23], dominates the long-lived coherence signals from a reaction center from the purple bacterium *Rhodobacter sphaeroides*. To clarify the origin of the coherence signal, a mutant bacterial reaction center (bRC), which has a much longer excited state lifetime the the wild type, was prepared. The chromophore assembly in the bRC protein complex is shown in Figure 3.1 with the absorption spectra. The six pigment molecules give rise to three well-separated Q_Y absorption bands. The EET among them occurs sequentially from H to B (~100 fs) and B to P (~250 fs) [24], followed by charge separation. The special pair (P) BChl dimer is an
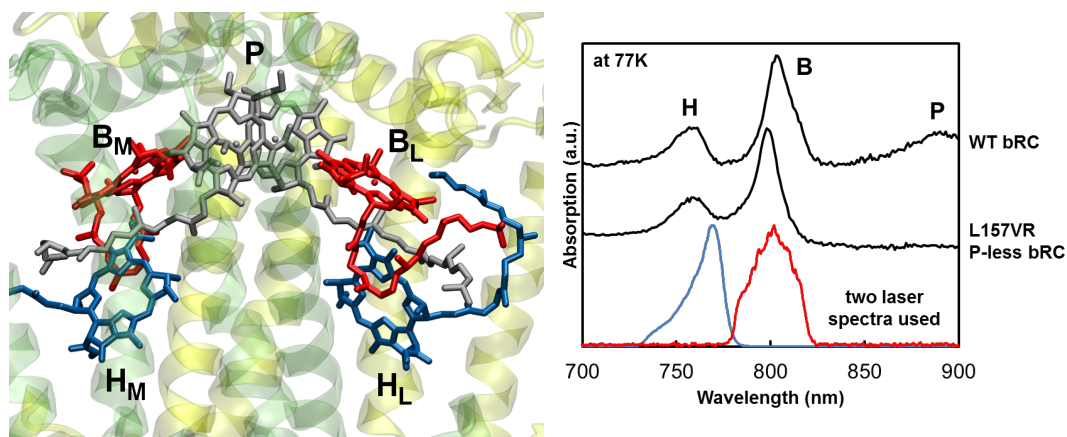
Figure 3.1: (left) The arrangement of chromophores responsible for the Q_Y region absorption in the bRC protein from Rhodobacter sphaeroides. (right) The 77K linear absorption spectra of two bRC samples (black) and the spectral profiles of the laser pulses (colored) used in the experiments. B and H bands correspond to the excitations on the accessory BChls (B_L and B_M) and the BPhys (H_L and H_M) molecules, respectively. The P band (from the special pair BChls) is only observed in the WT bRC. The 770 nm centered laser pulse was chosen to excite near zero-to-zero transtion for the H band.

efficient excitonic energy trap, and the excited state lifetime for B and H increases dramatically without it. A mutant bRC strain L157VR, which lacks two special pair BChls, was prepared to clarify the coherence component in the EET dynamics of bRC. The L157VR bRC does not have P dimer due to the replacement of VAL by ARG at L157 location. The binding pocket for the P dimer is occupied by the ARG residue to prevent binding of BChls molecules. The lack of the energy trap leads to an excited state lifetime nearing 1 ns for the B band [25].

To clarify the origin of the coherence signal, the polarization controlled two-color electronic coherence photon echo (2CECPE) technique was applied to study the B and H coherence in the bRC. The coherence related signals are often too weak to detect and obscured by other population related processes with higher signal strength. Currently there are two spectroscopic methods to suppress the pathways other than the coherence related ones. The 2DES with the coherence-specific polarizations utilizes the angle between chromophores to isolate coherence-related phenomena. The 2CECPE method separately excites two spectral regions, optically selecting only the coherence contributions. Because of these optically selective excitations in the 2CECPE, the investigated system will generate signal only if the two excited regions are coherently coupled. Here we combin the above two approaches to further delineate the participating physical processes in the coherence signal generation.

3.2 Assignment of the Coherence Signal to a Vibrational Origin

An electronic coherence requires the superposition of different excitonic states. Thus population in the corresponding excitonic states is an absolute prerequisite for the existance of electronic coherence. Due to the different excited state lifetimes between the wild type (WT) bRC and P-less mutant (L157VR) bRC, it can be expected that the electronic coherence lifetime between B and H would increase compared to the WT bRC.

Figure 3.2 shows the 2CECPE measurements of the WT and the P-less bRC. Despite very different excited state lifetimes of B in the two cases, the 2CECPE signals are similar to each other. Based on the purely electronic coupled dimer model, a simple interpretation would be that the $|B\rangle \langle H|$ electronic coherence persists for nearly 2 ps. However, this is physically impossible for the WT bRC because ultrafast EET from H and B to P depopulates H and B in ~300 fs after the initial excitation. The excited state lifetime for B and H has been well established by many transient absorption studies [24, 26, 25, 27]. The remaining excited state population
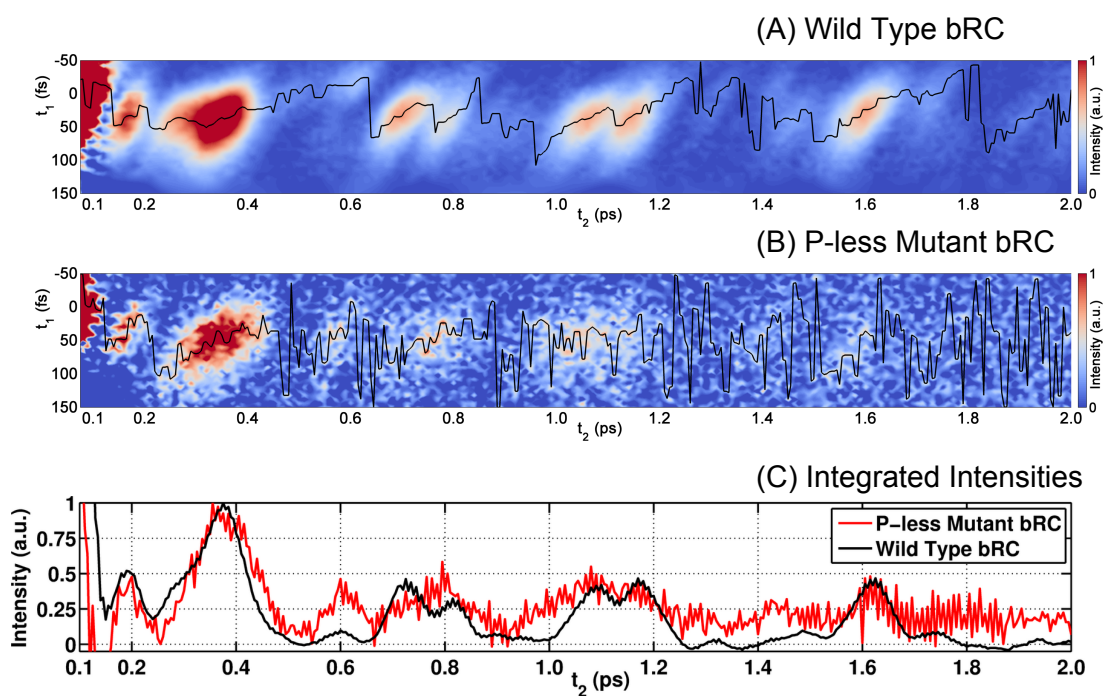
Figure 3.2: The 2CECPE integrated echo signals as a function of two time delays t_1 and t_2, from (A) WT bRC (B) P-less L157VR mutant bRC. (C) The integrated intensity of the each peak as a function of t_2. The t_2 axis represent the evolution of the initially prepared coherence. The data for $t_2 < 100$ fs are not shown because the photon echo signal related to the population pathway overwhelms the 2CECPE signal in this region due to the pulse overlap effect. The pulse ordering was 770 (k_1)-800 (k_2)-770 (k_3)-800 (k_s) (in wavelength).

for B and H can be estimated based on the known energy transfer timescale (H to B: 100 fs and B to P: 250 fs). A simple kinetic analysis predicts at most 1% of the initial populations would be left in H and B after 1.8 ps. The experimental signal intensity between late t_2 times and early t_2 times is much greater than 1% at 1.8 ps.

Even if we assume that the $|B\rangle \langle H|$ electronic coherence can generate strong enough signal despite the depopulation of excited B and H, this assumption cannot explain the mutant bRC data. The dynamics and lifetime of the electronic coherence is determined by two factors, the pure coherence dephasing and the population relaxations of the corresponding excitonic states[10]. Since the population relaxation in the P-less mutant bRC can be practically ignored in the observation time windows, it follows that the P-less mutant bRC should have a very different rapid electronic coherence dephasing mechanism, implying completely changed system-bath coupling to the protein environment. However, the similar B and H lineshapes in the absorption spectra between the WT and the P-less bRC indicates otherwise. Also, Stark spectroscopic studies on a P-less mutant confirm that the transition dipole moments for the H and B band were not largely affected by removing P, and circular dichroism (CD) spectra of a P-less mutant was also similar to the WT ones in that region [28]. Additionally, the protein structures for several mutant bRCs were found to be unaltered indicating the robustness of the bRC protein architecture [29]. A recent crystal structure study of cavity mutants, which do not carry a chromophore, also showed a similar result [30]. Although the crystal structure of the P-less L157VR mutant bRC has not been determined, it can be inferred that the proteins environment for B and H bands in the L157VR mutant bRC is very similar to that of the wild type. We now turn to an alternative model.

3.3   A Coupled Dimer with Vibrational Modes

The excitonic states of the chromophores can be considered as a coupled dimer due to the two well-separated absorption bands. Here a vibrational mode is explicitly assigned to each B and H excitonic state. The frequency of the vibration was chosen to be similar to the excitonic energy gap (~ 660 cm^{-1}) to satisfy the resonant condition with the excitation laser spectra. The corresponding ground state vibrational level $|g_1\rangle$ was also included.

Figure 3.3 displays the simple coupled dimer model with vibrational modes. All possible Feynman diagrams satisfying the excitation resonance condition show six newly available Liouville pathways in addition to the pure electronic coherence. The requirement for the 2CECPE signal is the coupling between the two excitation regions. There are only two additional transitions accessible due to the non-degenerate
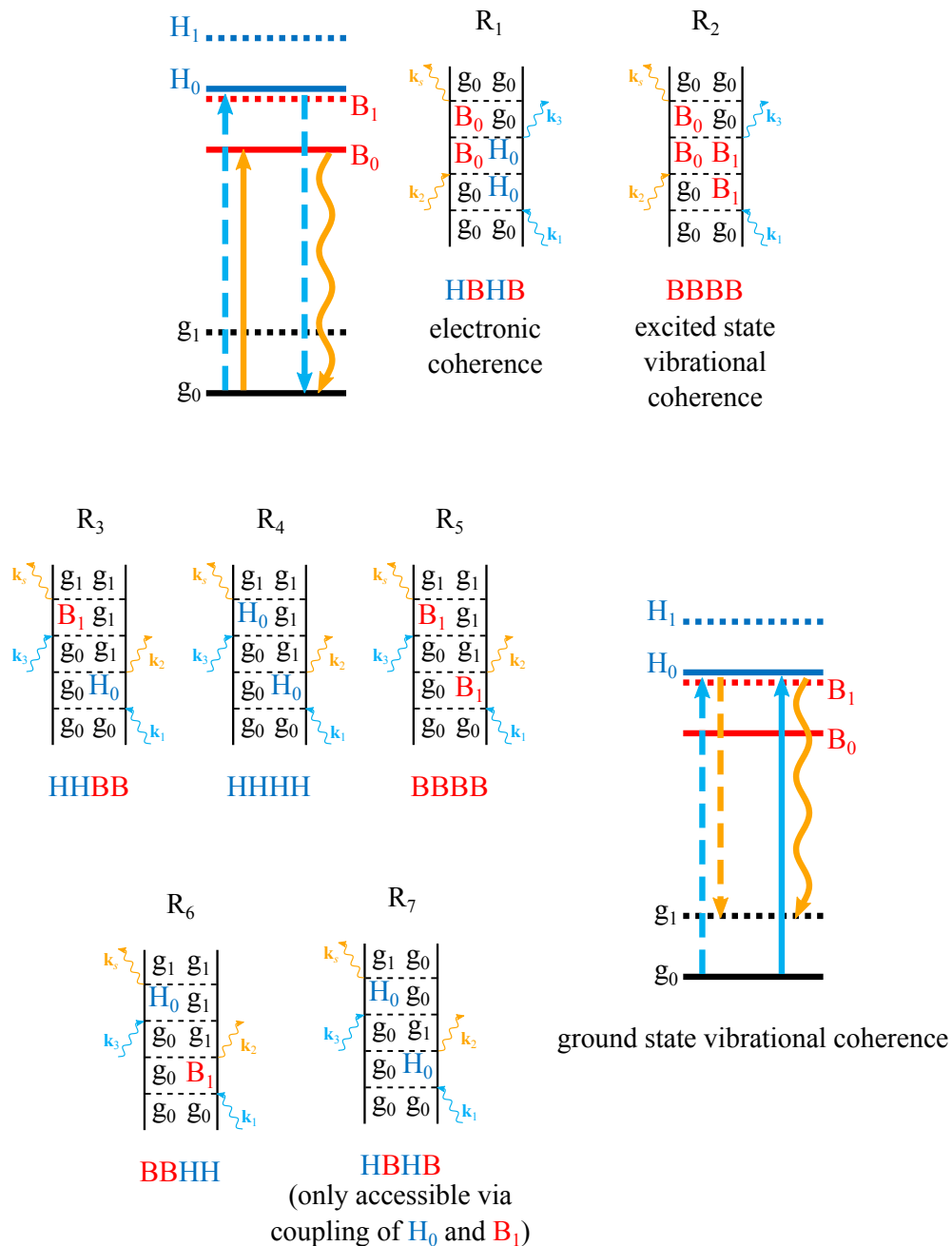
Figure 3.3: A coupled excitonic dimer model including a vibrational mode. The frequency of the vibration was chosen to be similar to the excitonic energy gap between B and H. All observable Liouville pathways ($R_1 \sim R_7$)are shown with their corresponding transition dipole interaction type. Color notation: (Red) B transition dipole moment (Blue) H transition dipole moment (Cyan) 770 nm laser pulse energy (Orange) 800 nm laser pulse energy

combination of the three laser pulse excitation wavelengths and the pulse ordering. The transitions to the higher vibrational level ($|g_0\rangle \rightarrow |B_1\rangle$) and the stimulated emission to the ground state ($|H_0\rangle \rightarrow |g_1\rangle$) allow vibrational coherences prepared during the t_2 time either on either the ground or excited states. No other transitions can be excited because either the transition energy is higher or lower than excitation spectrum allows, or the signal cannot be generated in the phase matching direction under the given pulse ordering (k_1-k_2-k_3). Even though other available pathways for the vibrational coherences were found by including a vibrational level in the model, it cannot be determined whether the observed vibrational coherence signal originates from an ground or excited state. In Figure 3.3 one can note that the interaction orders of the transition dipole moments are different for each pathway. The individual polarization control of excitation pulses can selectively suppress or enhance certain pathways highlighting a specific contribution to the signal. It will be explained below that the polarization controlled 2CECPE results only supports the R_7 pathway, indicating the vibronic coupling between the B and H excitonic states.

3.4   Polarization Dependent 2CECPE on WT bRC

Under the pure electronic dimer model, which does not consider any vibrational modes explicitly, each excitation pulse interacts with only one transition dipole moment. However, the model described in Figure 3.3 indicates that the H band is now composed of two different transition dipole moments: the zero-to-zero transition for the H exciton ($|g_0\rangle \rightarrow |H_0\rangle$) and the zero-to-one transition of the B exciton ($|g_0\rangle \rightarrow |B_1\rangle$). Despite the nearly degenerate energy levels, those two responses can be distinguished by the polarization control of excitation pulses because of the different origins of the two transition dipole moments.

The dependence of Liouville pathways on the linear polarizations of the laser pulse and relative orientations of transition dipole moments is described by a polarization prefactor, determined by Equation 3.1 [21] for an isotropic sample with orientational averaging.

$$
\begin{aligned}
&\left\langle \left(\hat{\alpha} \cdot \hat{E}_a\right) \left(\hat{\beta} \cdot \hat{E}_b\right) \left(\hat{\gamma} \cdot \hat{E}_c\right) \left(\hat{\delta} \cdot \hat{E}_d\right) \right\rangle \\
&= \frac{1}{30} \left\{ \cos\theta_{\alpha\beta} \cos_{\gamma\delta} \left(4\cos\theta_{ab}\cos\theta_{cd} - \cos\theta_{ac}\cos\theta_{bd} - \cos\theta_{ad}\cos\theta_{bc}\right) \right. \\
&\quad + \cos\theta_{\alpha\gamma} \cos_{\beta\delta} \left(-\cos\theta_{ab}\cos\theta_{cd} + 4\cos\theta_{ac}\cos\theta_{bd} - \cos\theta_{ad}\cos\theta_{bc}\right) \\
&\quad \left. + \cos\theta_{\alpha\delta} \cos_{\beta\gamma} \left(-\cos\theta_{ab}\cos\theta_{cd} - \cos\theta_{ac}\cos\theta_{bd} + 4\cos\theta_{ad}\cos\theta_{bc}\right) \right\} \quad (3.1)
\end{aligned}
$$

Table 3.1: The calculated polarization prefactor for the polarization sequences used in the experiments. The two transition dipole moments were assumed to be orthogonal.

	Polarization Configuration				Transition Dipole Interaction Orders		
	k_1	k_2	k_3	k_s	HHHH/BBBB	HHBB/BBHH	HBHB
<1>	0	0	0	0	1/5	1/15	1/15
<2>	$\pi/4$	$-\pi/4$	$\pi/2$	0	0	0	1/12
Relevant Feynman Diagram:					R_2, R_4, R_5	R_3, R_6	R_1, R_7

Here the indexes of a, b, c, d are the light polarizations in the lab frame and α, β, γ and δ are the excited state transition dipole moments in the molecular frame. For example, θ_{ab} represents the relative polarization angle difference between $\hat{E}_a$ and $\hat{E}_b$, and $\theta_{\alpha\beta}$ represents the projection angle between the two transition dipoles of α and β. The angle between the transition dipole moments can be expressed more explicitly as in Equation 3.2.

$$\hat{\mu}_\alpha \cdot \hat{\mu}_\beta = |\mu_\alpha| \, |\mu_\beta| \cos \theta_{\alpha\beta} \tag{3.2}$$

Once the linear polarizations excitation pulses are determined, the polarization prefactors can be calculated for a dimer with an fixed projection angle. The calculated prefactors are summarized in Table 3.1 and the corresponding Liouville pathways in Figure 3.3 are noted. The calculation assumes that B and H excitonic states transition dipole moments are orthogonal (projection angle 90°).

The 2CECPE spectra of the WT bRC taken with the coherence specific polarization configuration [31, 32] $(\frac{\pi}{4}, -\frac{\pi}{4}, \frac{\pi}{2}, 0)$ is shown in Figure 3.4. Compared to the all parallel polarization spectra shown in Figure 3.2, the changes are minor, implying all the coherence signal originates from the HBHB type of the transition dipole interaction. Noticeable changes are observed in the decreased amplitude of the first peak at $t_2 = 150$ fs and the absence of the peak with small amplitude at $t_2 = 600$ fs. Also the amplitudes of the peaks between $t_2 = 700$ fs and 1300 fs are stronger when compared to the peak with the strongest intensity at $t_2 = 350$ fs. Under the coherence specific polarization condition the only two pathways that give rise to the 2CECPE signal are the electronic coherence (R_1) and the ground state vibrational coherence via nonadiabatic vibronic coupling (R_7). However, the ground state vibrational coherence is the dominant contribution to the coherence signal, especially for $t_2 > 300$ fs, since the remaining electronic coherence would be negligibly small due to the fast depopulation of B and H.
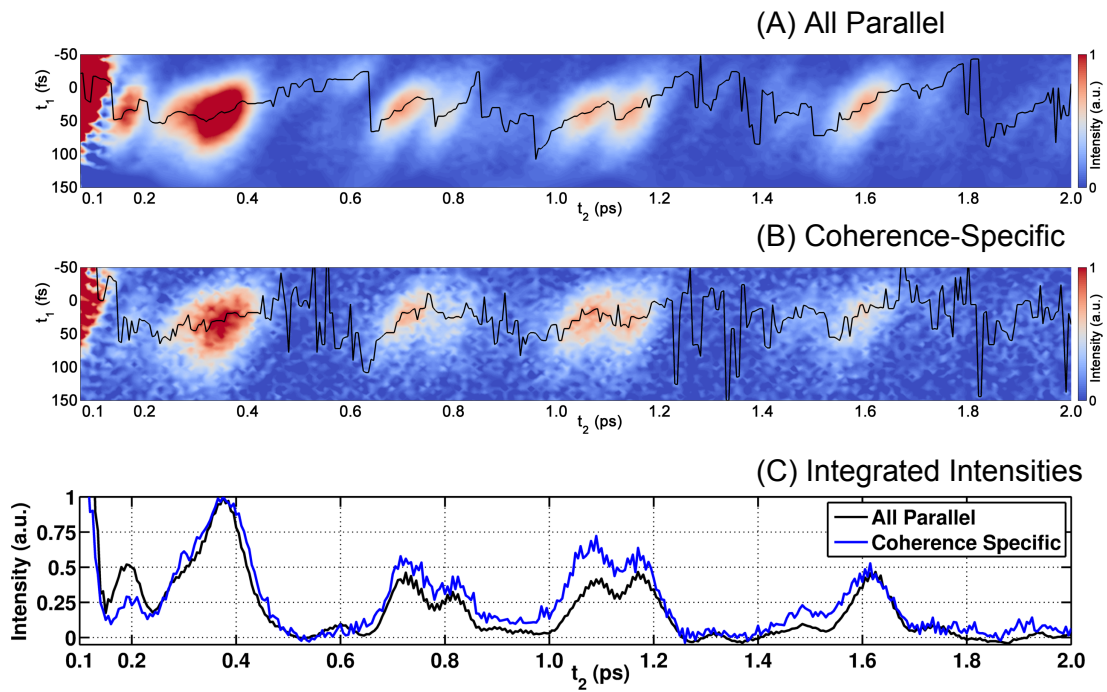
Figure 3.4: The 2CECPE integrated echo signals from WT bRC under two different polarization sequences (A) All parallel (0,0,0,0) (B) coherence specific $(\frac{\pi}{4}, -\frac{\pi}{4}, \frac{\pi}{2}, 0)$ (C) Integrated peak intensities for (A) and (B). The pulse ordering was 770 (k_1)-800 (k_2)-770 (k_3)-800 (k_s) (in wavelength).

3.5   Discussion

The combination of the 2CECPE and the polarization control strictly limits the possible Liouville pathway for the given phase matching direction with a fixed pulse ordering. Under the resonance condition provided by the spectra of two different laser pulses and the coherence specific polarization used above, signals arise only from the HBHB type of the interaction. Thus the system must have a physical mechanism to couple the H and B transition dipole moments. As electronic coherence cannot be such mechanism except at early duration of t_2 times, the above observation suggests that a nonadiabatic vibrational-excitonic coupling is present between B and H. The nonadiabatic interaction of two excitonic states was recently explored theoretically and identified an anti-correlated vibration between the two pigments as the key component to facilitate the nonadiabatic interaction [23]. Such vibrational motion in one molecule is countered by the other molecule's motion in the opposite direction, and tunes the potential energy difference to drive nonadiabatic dynamics. This framework for the coupled dimer system enables the R_7 pathway described in Figure 3.3, and the consequently created the ground state vibrational coherence created mimics many signatures of electronic coherence in reported 2DES spectra.

For the bacterial reaction center, the pigments in B bands, i.e. accessory bacteriochlrophylls should have vibrational mode whose frequency is similar to the B and H excitonic energy gap. The excitonic energy gap for B and H is estimated to be around 660 cm^{-1} (peak to peak difference of H and B bands from the absorption spectrum), and a resonance Raman studies on WT bRC from *Rhodobacter sphaeroides* reported four vibrational modes near 660 cm^{-1}: 566, 621, 682, 721 cm^{-1}[33]. The broad lineshape of the two bands introduces uncertainties in determining one specific vibrational mode responsible, any one of these can be coupled to the zero-to-zero transtion of H band. The calculation showed that the range of a frequency to drive the nonadiabatic interaction for a certain excitonic energy gap value is rather broad (± 40 cm^{-1})[23]. Therefore the presence of a vibrational mode nearly matching excitonic energy gap is sufficient to activate the vibrational-electronic coupling between the B and H bands.

The oscillating frequency components are found by Fourier transfrom of the time traces are shown in Figure 3.5. There are two possible origins for the frequencies. The first one is a set of low frequency vibrations coherently excited as a spectator mode. Such coherent low frequency vibrations will modulate the signal and their frequencies will be directly reflected to the signal. The second possibility is the difference between two high frequencies. Due to the two different applied wavelengths and the integrated homodyne detection in the 2CECPE, any two high frequencies
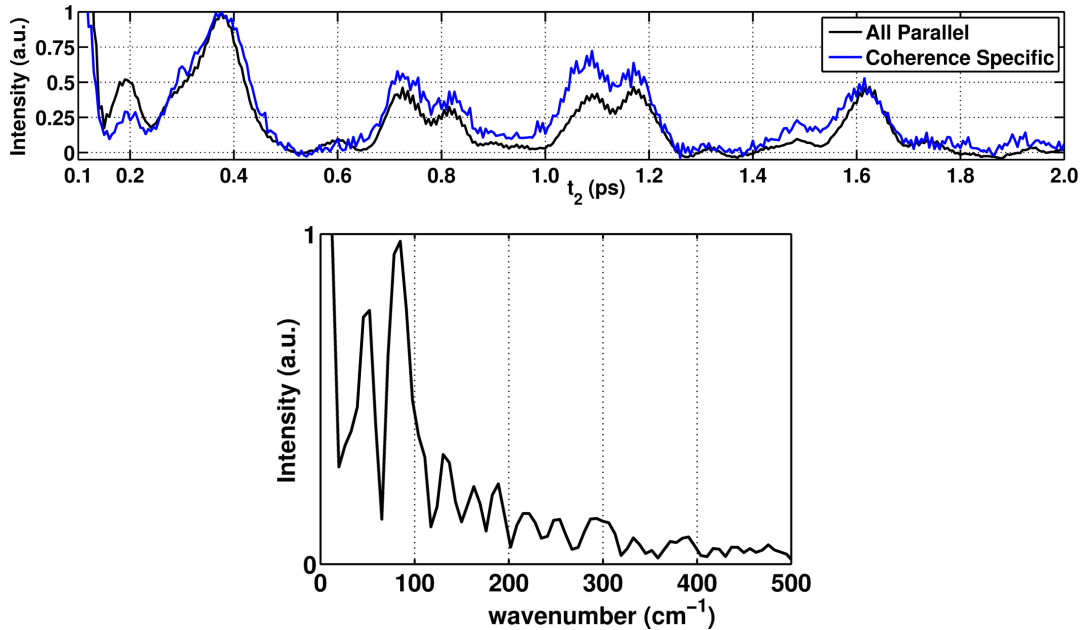
Figure 3.5: The time trace along the t_2 of 2CECPE spectrum of WT bRC and its Fourier transfrom. The two low frequencies are found to be 90 and 50 cm^{-1}.

near the energy difference of laser spectra will provide such low frequencies. This can be further clarified by the heterodyned 2CECPE, namely two-color 2DES, because their frequencies will be directly observed in the signal modulation along the t_2 time.

Given that the 2CECPE signal amplitudes are not largely altered by the coherence specific polarization compared to the all parallel polarization configuration, it can be established that other Liouville pathways ($R_2 \sim R_6$) contribute minimally to the coherence signal. A notable difference is that the peak at $t_2 = 600$ fs is absent in the coherence specific polarization sequence, and the origin of this peak can be determined by the comparison to the P-less mutant data. One interesting aspect of the peak at $t_2 = 600$ fs is that it is positioned near $t_1 \sim 0$, while other peaks are located near $t_1 \sim 40$ fs in the WT bRC. However, in the P-less mutant bRC, there is no such shift toward $t_1 = 0$ for the peak at 600 fs. In terms of the integrated photon echo signal, the intensity maximum position along t_1 axis is correlated to the inhomogeneity of the chromophore surrounding environment and generally decays and time delay between the second and the third pulse increases[15]. In this framework, it can be inferred that the different shift along t_1 axis reflects different dynamics between the WT and mutant bRCs. Among the Liouville pathways that are suppressed by the coherence specific polarization, the only pathway that is affected by

the dynamics in the bRC is the B excited state vibrational coherence pathway (R_2). An excited state vibrational coherence contains aspects of both electronic and vibrational coherence decay. According to the same simple kinetic analysis, about 10% of the initial excitation population still exist at 600 fs after on B, and this is enough to generate the observed small amplitude signal. In this sense, the signal amplitude should be stronger in the P-less mutant due to the longer excited state lifetime, and this is exactly what is observed in Figure 3.2. The shift of the peak in decreasing t_1 value direction observed in the WT bRC may be the effect of the formation of the charge separation state following the energy transfer. Such shift is absent in the P-less mutant bRC because there is no charge separation due to the removed special pair dimer[25].

The question on how much of the coherence signal from the coherence-specific 2CECPE can be accounted for the electronic coherence is important. Although it is clear that the signals at the late t_2 times are from the ground state vibrational coherence, it is difficult to quantitatively draw a clear line between the electronic coherence and the ground state vibrational coherence. The initial peak with the weak amplitude at $t_2 = 200$ fs and the strongest signal at $t_2 = 400$ fs are most likely the mixture of the electronic coherence and the ground state vibrational coherence contributions, but more quantitative modeling would be necessary to further extract exact electronic coherence lifetime. A traditional probe for the electronic coherence is the beating in anisotropy decay. The decay in anisotropy beating for B and H was measured to be ~100 fs [27]. While previous 2CECPE study suggested near 300 fs lifetime for B and H electronic coherence. Further studies would be needed to clarify pure electronic coherence contribution.

3.6   Conclusion

A combination of 2CECPE and the polarization control demonstrated its capability to further distinguish the specific origin of the coherence related signals. The complexity in the observed coherence signals clearly indicate that the electronic coherence is not sufficient to explain all the features, and vibrational contributions should be considered.

The polarization controlled 2CECPE data, in combination to the coupled dimer model with vibrational modes, suggest that a coupling between a vibrational mode (B_1) and the nearby electronic state (H_0) is neccessary to create the ground state vibrational coherence. Also observed low frequency oscillations indicate there are multiple vibrational modes associated to the coupling mechanism. A study indicated that energy relxation can occur without the destruction of vibrational phase

leading to the coherent motion in the final state below the curve crossing region [34]. Another recent study indicated that a specific anti-correlated vibrational motion may provide such electronic-vibrational coupling [23]. Further theoretical studies would be neccesary to identify the exact nature of electronic-vibrational coupling in photosynthetic EET processes. A combination of 2CECPE and the polarization control demonstrated its capability to further distinguish the specific origin of coherence related signals. Further applications of the 2CECPE on other PPCs may provide more information on the rolf of electronic and vibrational coherences in excitation energy transfer.

3.7 Experimental Details

The His-tagged bRC from Rhodobacter sphaeroides was prepared based on the previous description [35]. Cells cultured in dark and semi-aerobic condition were harvested and homogenized. The bRC proteins were solubilized by the lauryldimethylamine oxide (LDAO) and purified with a Ni-NTA column followed by FPLC. The samples were prepared in a glycerol/buffer (10 mM Tris HCl at pH 8.0 with 0.5 % LDAO) (60/40, v/v) mixture placed between quartz windows, and cooled to 77 K using a cryostat (Oxford Instruments). The optical density at 800 nm was 0.2~0.3 at 77 K with a 0.2 mm path length. Sodium dithionite ($Na_2S_2O_4$) was added to a concentration of 5 mM for the WT bRC experiment to avoid the accumulation of P^+cation [36].

A commercial regenerative amplifier (Coherent) running at 1 KHz provided 800 nm pulses and pumped an optical parametric amplifier (Coherent) to generated 770 nm pulses. Optical filters with the 25 nm bandwidth were used to prevent the spectral overlap between the pulses of two different center wavelengths. Three pulses, arranged in equilateral triangle geometry, were focused onto the sample with the pulse energy of 6 nJ for each. The time-integrated photon echo signals, as a function of t_1 and t_2, was collected with a photomultiplier tube (Hamamatsu) using the lock-in amplification with an optical chopper. An optical bandpass filter centered at 800 nm with 25 nm bandwidth was placed in front of the photomultiplier tube to detect signals from the coherence pathways only. For the polarization dependent experiments, a linear polarizer was placed along each laser beam travelling path. An additional fourth linear polarizer was placed in front of the photomultiplier tube as an analyzer. The contrast ratio of each polarizer was found to be 1000:1 within the error of $\pm 1°$.

Bibliography

[1] G. S. Engel, T. R. Calhoun, E. L. Read, T.-K. Ahn, T. Mancal, Y.-C. Cheng, R. E. Blankenship, and G. R. Fleming, *Nature* **446**, 782 (2007).

[2] E. Collini, C. Y. Wong, K. E. Wilk, P. M. G. Curmi, P. Brumer, and G. D. Scholes, *Nature* **463**, 644 (2010).

[3] H. Lee, Y.-C. Cheng, and G. R. Fleming, *Science* **316**, 1462 (2007).

[4] G. D. Scholes, G. R. Fleming, A. Olaya-Castro, and R. van Grondelle, *Nat. Chem.* **3**, 763 (2011).

[5] R. E. Blankenship, *Molecular Mechanisms of Photosynthesis*, Blackwell Science, 2002.

[6] M. Gouterman, G. H. Wagnière, and L. C. Snyder, *J. Mol. Spectrosc.* **11**, 108 (1963).

[7] M. Kobayashi, S. Ohashi, K. Iwamoto, Y. Shiraiwa, Y. Kato, and T. Watanabe, *Biochim. Biophys. Acta* **1767**, 596 (2007).

[8] H. van Amerongen, L. Valkunas, and R. van Grondelle, *Photosynthetic Excitons*, World Scientific: Singapore; River Edge, N.J., 2000.

[9] D. Noy, C. C. Moser, and P. L. Dutton, *Biochim. Biophys. Acta* **1757**, 90 (2006).

[10] Y.-C. Cheng and G. R. Fleming, *Annu. Rev. Phys. Chem.* **60**, 241 (2009).

[11] A. Ishizaki and G. R. Fleming, *Annual Review of Condensed Matter Physics* **3**, 333 (2012).

[12] W. Zinth and J. Wachtveitl, *ChemPhysChem* **6**, 871 (2005).

[13] J. ALLEN and J. WILLIAMS, *FEBS Lett.* **438**, 5 (1998).

[14] S. MUKAMEL, *Principles of Nonlinear Optical Spectroscopy*, Oxford University Press, USA, 1999.

[15] G. R. FLEMING and M. CHO, *Annu. Rev. Phys. Chem.* **47**, 109 (1996).

[16] M. CHO and G. R. FLEMING, *J. Chem. Phys.* **123**, 114506 (2005).

[17] T. MANCAL and G. R. FLEMING, *J. Chem. Phys.* **121**, 10556 (2004).

[18] D. Y. PARKINSON, H. LEE, and G. R. FLEMING, *J. Phys. Chem. B* **111**, 7449 (2007).

[19] B. S. PRALL, D. Y. PARKINSON, and G. R. FLEMING, *J. Chem. Phys.* **123**, 054515 (2005).

[20] M. SAROVAR, A. ISHIZAKI, G. R. FLEMING, and K. B. WHALEY, *Nat. Phys.* **6**, 462 (2010).

[21] R. M. HOCHSTRASSER, *Chem. Phys.* **266**, 273 (2001).

[22] G. D. SCHOLES, *J. Chem. Phys.* **121**, 10104 (2004).

[23] V. TIWARI, W. K. PETERS, and D. M. JONAS, *Proc. Natl. Acad. Sci. U. S. A.* **110**, 1203 (2013).

[24] M. H. VOS, J. BRETON, and J.-L. MARTIN, *J. Phys. Chem. B* **101**, 9820 (1997).

[25] J. A. JACKSON, S. LIN, A. K. W. TAGUCHI, J. C. WILLIAMS, J. P. ALLEN, and N. W. WOODBURY, *J. Phys. Chem. B* **101**, 5747 (1997).

[26] Y. JIA, D. M. JONAS, T. JOO, Y. NAGASAWA, M. J. LANG, and G. R. FLEMING, *J. Phys. Chem* **99**, 6263 (1995).

[27] D. C. ARNETT, C. C. MOSER, P. L. DUTTON, and N. F. SCHERER, *J. Phys. Chem. B* **103**, 2014 (1999).

[28] L. MOORE and S. BOXER, *Photosynth. Res.* **55**, 173 (1998).

[29] A. J. CHIRINO, E. J. LOUS, M. HUBER, J. P. ALLEN, C. C. SCHENCK, M. L. PADDOCK, G. FEHER, and D. C. REES, *Biochemistry* **33**, 4584 (1994).

[30] P. K. Fyfe, J. a. Potter, J. Cheng, C. M. Williams, A. J. Watson, and M. R. Jones, *Biochemistry* **46**, 10461 (2007).

[31] M. T. Zanni, N. H. Ge, Y. S. Kim, and R. M. Hochstrasser, *Proc. Natl. Acad. Sci. U. S. A.* **98**, 11265 (2001).

[32] G. S. Schlau-Cohen, A. Ishizaki, T. R. Calhoun, N. S. Ginsberg, M. Ballottari, R. Bassi, and G. R. Fleming, *Nat. Chem.* (2012).

[33] N. J. Cherepy, a. P. Shreve, L. J. Moore, S. G. Boxer, and R. a. Mathies, *Biochemistry* **36**, 8559 (1997).

[34] J. M. Jean and G. R. Fleming, *J. Chem. Phys.* **103**, 2092 (1995).

[35] J. O. Goldsmith and S. G. Boxer, *Biochim. Biophys. Acta* **1276**, 171 (1996).

[36] B. A. King, T. B. McAnaney, A. de Winter, and S. G. Boxer, *Chem. Phys.* **294**, 359 (2003).